Nano Research
2020, 13(8): 2299–2307
ISSN 1998-0124 CN 11-5974/O4
https://doi.org/10.1007/s12274-020-2850-5

Research Article

Oxygen defects boost polysulfides immobilization and catalytic conversion: First-principles computational characterization and experimental design

Qiu He[1], Bin Yu[1], Huan Wang[1], Masud Rana[2], Xiaobin Liao[1], and Yan Zhao[1,3] (✉)

[1] *State Key Laboratory of Silicate Materials for Architectures, International School of Materials Science and Engineering, Wuhan University of Technology, Wuhan 430070, China*
[2] *Materials Engineering, School of Mechanical and Mining Engineering, The University of Queensland, St Lucia, QLD 4072, Australia*
[3] *The Institute of Technological Sciences, Wuhan University, Wuhan 430072, China*

Received: 19 December 2019/ **Revised:** 16 April 2020 / **Accepted:** 2 May 2020

ABSTRACT

Although some experiments have shown that point defects in a cathode host material may enhance its performance for lithium-sulfur battery (LSB), the enhancement mechanism needs to be well investigated for the design of desired sulfur host. Herein, the first principle density functional theory (DFT) is adopted to investigate a high-performance sulfur host material based on oxygen-defective TiO_2 (D-TiO_2). The adsorption energy comparisons and Gibbs free energy analyses verify that D-TiO_2 has relatively better performances than defect-free TiO_2 in terms of anchoring effect and catalytic conversion of polysulfides. Meanwhile, D-TiO_2 is capable of absorbing the most soluble and diffusive long-chain polysulfides. The newly designed D-TiO_2 composited with three-dimensional graphene aerogel (D-TiO_2@Gr) has been shown to be an excellent sulfur host, maintaining a specific discharge capacity of 1,049.3 mAh·g^{-1} after 100 cycles at 1C with a sulfur loading of 3.2 mg·cm^{-2}. Even with the sulfur mass loading increasing to 13.7 mg·cm^{-2}, an impressive stable cycling is obtained with an initial areal capacity of 14.6 mAh·cm^{-2}, confirming the effective enhancement of electrochemical performance by the oxygen defects. The DFT calculations shed lights on the enhancement mechanism of the oxygen defects and provide some guidance for designing advanced sulfur host materials.

KEYWORDS

oxygen defects, catalytic conversion, lithium-sulfur battery, density functional theory

1 Introduction

Lithium-sulfur battery (LSB) is emerging as one of the next-generation high-performance energy storage device, owing to its high theoretical capacity (1,675 mAh·g^{-1}) and the abundant low-toxicity sulfur resources [1–5]. However, the industrial applications of LSB still need extensive research and developments to overcome its intrinsic limitations, including the low electronic/ionic conductivity of Li_2S/S (electronic resistivity > 10^{14} ohm·cm; Li^+ diffusivity ≈ 10^{-13}/5 × 10^{-30} S·cm^{-1}), the large volume change of the cathode, the dissolution/diffusion of lithium polysulfides (so called "shuttle effect"), the sluggish reaction kinetics, and the low reaction potential (~ 2.15 V) [6–8]. In general, conductive and porous host materials, such as porous carbonaceous materials, can serve as electron transfer network, and provide the buffer space for volume expansion [9, 10]. However, the intrinsic non-polar carbon has limited anchoring effects (0.1–0.7 eV) to polysulfides and can hardly accelerate the reaction kinetics [11]. The best solution for the LSB cathode is to find suitable host materials with both powerful immobilization and catalytic conversion capabilities of polysulfides, which is one of the main requirements for LSB [12–15]. Moreover, owing to the low reaction potential of LSB, it is necessary to have a high mass loading of active sulfur to achieve a high areal capacity. In order to compete with commercial lithium ion battery (LIB), the areal capacity of LSB should at least be 4 mAh·cm^{-2} [16, 17]. This areal capacity is proportionally dependent on the sulfur loading in LSB. However, a high sulfur loading results in a thick electrode, leading to the deterioration of conductivity, mechanical property, and capacity retention. Therefore, the design of promising host materials with high areal capacity remains to be a tough challenge.

As mentioned above, a high-performance host material for LSB cathode should have both polysulfides trapping and catalytic conversion capabilities. For this purpose, many research groups have investigated the potential applications of polar compounds as the sulfur host materials, such as transitional metal oxides/nitrides/sulfides/borides/carbides/phosphides [18–27]. In general, it is difficult for a single compound to possess those two capabilities simultaneously, and several research groups have made progresses by combining different materials to form a functional heterojunction structure. Yang's group [28] have constructed twin-born TiO_2-TiN heterostructure separator for LSB, in which TiO_2 is for confining polysulfides and TiN is for accelerating polysulfides conversion. The synergistic effect is highly efficient for both polysulfides confinement and catalytic conversion. Recently, a similar

Address correspondence to yan2000@whut.edu.cn

structure of VO_2-VN was reported [29], and it was shown to be a successful sulfur host for LSB, demonstrating the effectiveness of the heterostructure approach. However, the fabrication of a heterostructure is a complicated process and it sometimes compromises the capability of each component. Accordingly, it is interesting to see if we can use defect engineering to design a single compound with both the polysulfides trapping and catalytic conversion capabilities. Defects engineering is widely used to design functional materials with active sites of enriched electrons. Moreover, nonmetallic atomic defects can enhance the conductivity of the host materials, and many of the defects-engineered materials were reported to be superior to their defect-free counterparts in confining polysulfides and accelerating polysulfides conversion [30–33]. However, the atomic level interactions of defects with polysulfides and the catalytic conversion processes are hard to be characterized even with high-resolution testing technology, while they are of great significance for applications [34]. Furthermore, most of the previous studies employed a large portions of metal compounds, which results in undesirable low sulfur mass loading (< 2 mg·cm^{-2}), hindering the practical application of LSB [35].

To comprehensively illustrate the defects function mechanisms of host materials for sulfur cathode in atomic level, herein, we chose the defect-engineered TiO_2 (D-TiO_2) as an object to explore the effects of oxygen defects on polysulfides adsorption and catalytic conversion by means of density functional theory (DFT) calculations. Our calculations show that D-TiO_2 has distinctively higher polysulfide adsorption energies than the defect-free TiO_2, especially for the most soluble and diffusive long-chain polysulfides (Li_2S_6, Li_2S_8). Meanwhile, DFT Gibbs free energy analyses confirm that the polysulfides conversion is thermodynamically more favorable on the D-TiO_2 surface than on the defect-free TiO_2 surface. Therefore, the oxygen defects in TiO_2 are extremely beneficial in terms of anchoring effect and catalytic conversion of polysulfides. Based on our DFT calculations, we designed a sulfur host by integrating the oxygen-defective TiO_2 nanosheets with three-dimensional (3D) graphene (D-TiO_2@Gr). The highly conductive and porous 3D Gr provide a rapid electron transport network, and abundant space for sulfur loading as well as the volume buffering during cycling. The assembled LSB achieves high capacity retention, good rate capability, and especially high sulfur mass loading. The capacities of 1,049.3 mAh·g^{-1} after 100 cycles at 1C and 582.4 mAh·g^{-1} after 450 cycles at 2C are delivered, corresponding to the decay rate of only 0.094% and 0.069% per cycle, respectively. When tested with much higher sulfur loading of 13.7 mg·cm^{-2}, D-TiO_2@Gr delivers an impressively high areal capacity of 10.9 mAh·cm^{-2} at a current density of 4.6 mA·cm^{-2} after 50 cycles. The overall improvement of electrochemical performance promotes the practical application of LSB and the strategy of defect-engineering provides an alternative way of functionalizing materials for the LSB system.

2 Methodology and experimental section

2.1 Synthesis of defective TiO_2@Gr

The 3D ascorbic acid reduced graphene oxide was fabricated following the experimental process in a previous paper [36], and the TiO_2 nanosheets were synthesized by a sol-gel method followed by a hydrothermal process [37]. The condensed Gr suspension was diluted to 1 M (suspension A). Subsequently, 1.5 mg of TiO_2 nanosheets powders were homogeneously dispersed into suspension A, followed by a hydrothermal process at 95 °C for ~ 2 h. The resultant defect-free TiO_2@Gr aerogel was washed by DI water for three times. The aerogel was freeze-dried for 48 h, then dried in oven at 70 °C for 8 h. The defect-free TiO_2@Gr aerogel was finally annealed at 500 °C in Ar/H_2 (95%:5%, v/v) flow gas for 2 h to obtain D-TiO_2@Gr aerogel. The pure TiO_2 powders and pure 3D Gr aerogel were treated with the same annealing process as D-TiO_2@Gr, and they were used as the control samples.

2.2 Preparation of Li_2S_6 electrolyte

The Li_2S_6 electrolyte was synthesized by resolving the sulfur and Li_2S powders with a molar ratio of 5:1 into liquid mixture of 1,2-dimethoxyethane (DME, 99.5%) and 1,3-dioxolane (DOL, 99.5%) (1:1, v/v) with 1 M lithium bis (trifluoromethanesulfonyl) imide (LiTFSI), following by vigorously stirring on a homothermal magnetic stirrer at ~ 70 °C for 48 h.

2.3 Structural characterizations

The X-ray diffraction (XRD) characterization was carried out using an X-ray diffractometer with a non-monochromated Cu Kα X-ray source (Bruker D8 Advance). The scanning electron microscopy (SEM) images were collected by electric microscopes (JEOL JSM-7100F and Titan G2 60-300). The energy-dispersive X-ray spectra (EDS) were recorded using an Oxford IE250 system. The transmission electron microscopy (TEM) and high resolution TEM (HRTEM) images were recorded with a Titan G2 60-300 instrument with EDS image corrector. The thermogravimetric (TG) curves were obtained from a thermal analyzer (Netzsch STA 449C), and the X-ray photoelectron spectroscopy (XPS) measurements were conducted using a VG MultiLab 2000 instrument. The electron paramagnetic resonance (EPR) measurement was conducted with a Bruker EMX Plus spectrometer using an X band (9.78 GHz) at room temperature. Scanning transmission electron microscopy (STEM) and electron energy loss microscopy (EELS) were operated on a FEI Titan microscope with a CEOS probe aberration-corrector operated at 200 keV.

2.4 LSB cell assembly

The stainless-steel coin cells (CR2025-type) were assembled in a glovebox filled with argon. The electrolyte was 1.0 M LiTFSI dissolved in DOL and DME (1:1, v/v) with 0.1 M lithium nitrate ($LiNO_3$, 99.9%) as the additive. Li_2S_6 electrolyte was dropped into self-supported sulfur hosts as the sulfur source. The sulfur mass loading is controlled by the amount of Li_2S_6 electrolyte added to the D-TiO_2@Gr host material. In normal tests, the total amount of electrolyte added to each battery was 25 μL. In the tests of LSBs with high sulfur loadings of 6.8, 10.2, and 13.7 mg·cm^{-2}, the contents of electrolyte were 35, 45, and 55 μL, corresponding to the sulfur contents of 75.4%, 82.2%, and 86%, respectively. A commercial Celgard polypropylene membrane was employed as the separator. The as-synthesized D-TiO_2@Gr aerogel was directly used as the self-supported sulfur host.

2.5 Electrochemical tests

The galvanostatic charge-discharge, cyclic, and rate performance tests were carried out with a battery testing system (LAND CT2001A). The cyclic voltammetry (CV), open-circuit curves (OCV) and electrochemical impedance spectroscopy (EIS) were performed with the CHI 600e electrochemical workstation and Autolab PGSTAT 302N.

2.6 First-principles calculation

All the first-principles DFT calculations have been performed

with the Vienna *ab-initio* simulation package (VASP) [38], using the Perdew-Burke-Ernzerhof (PBE) exchange-correlation functional [39] and the projector augmented wave (PAW) method [40]. The plane wave cutoff energy was set to be 550 eV, the electronic self-consistent convergence is 1×10^{-5} eV/atom and the force threshold for the geometry optimization is 0.02 eV·Å^{-1}. For the surface related calculations, a $2 \times 2 \times 1$ Gamma centered k mesh was employed, and the van der Waals (vdW) force was taken into consideration based on Grimme's dispersion correction method version 3 (DFT-D3) [41]. DFT-D3, as the last major version of DFT-D method, is close to the limit of "nonelectronic" approach for computing the dispersion energy, and it can be coupled with any standard density functional and applied to any element and most systems. For the transitional state search calculations, the k mesh was set as $2 \times 2 \times 2$ and the climbing-image nudged elastic band (CINEB) method was used [42].

The most stable surface of anatase TiO_2 (101) was determined by the surface energy calculations, and different configurations of Li_2S adsorbed on TiO_2 (101) were tested to explore the interactions of Li_2S and TiO_2 surface and to determine the most attractive site on TiO_2 surface. Based on the exploration, the configurations of other polysulfides/S_8 adsorbed on TiO_2 were constructed to obtain the adsorption energy.

The specific surface energy (γ_s), an oxygen defect formation energy (E_d) and adsorption energy (E_a) were calculated by the following equations

$$\gamma_s = \frac{1}{2A}\left(E(Ti_xO_y) - xE(TiO_2) - \left(\frac{1}{2}y - x\right)E(O_2)\right) \quad (1)$$

$$E_d = E(Ti_xO_{y-1}) + \frac{1}{2}E(O_2) - E(Ti_xO_y) \quad (2)$$

$$E_a = E(TiO_2{+}Li_2S_x) - E(TiO_2) - E(Li_2S_x) \quad (3)$$

In Eq. (1), A is the cross-sectional area of the slab. The elementary reactions for the reduction of S_8 to Li_2S were listed below. The star "*" refers to the state of being absorbed, whereas the isolated state does not have a star mark. For Gibbs free energy calculations, the energy of ($Li^+ + e^-$) was calculated as the energy of a Li atom in the Li metal.

$$S_8 + 16Li^+ \rightarrow S_8^* + 16Li^+ \quad (4)$$

$$S_8^* + 16Li^+ + 2e^- \rightarrow Li_2S_8^* + 14Li^+ \quad (5)$$

$$Li_2S_8^* + 14Li^+ + 2e^- \rightarrow Li_2S_6^* + Li_2S_2 + 12Li^+ \quad (6)$$

$$Li_2S_6^* + Li_2S_2 + 12Li^+ + 2e^- \rightarrow Li_2S_4^* + 2Li_2S_2 + 10Li^+ \quad (7)$$

$$Li_2S_4^* + 2Li_2S_2 + 10Li^+ + 2e^- \rightarrow Li_2S_2^* + 3Li_2S_2 + 8Li^+ \quad (8)$$

$$Li_2S_2^* + 3Li_2S_2 + 8Li^+ + 8e^- \rightarrow Li_2S^* + 7Li_2S \quad (9)$$

3 Results and discussions

3.1 First-principles computational characterization of D-TiO_2

In order to explore the effects of oxygen defects for the enhancement of polysulfides immobilization and catalytic conversion, we employed DFT to simulate the polysulfides adsorption kinetics and catalytic conversion process on the anatase TiO_2 surface. The surface energies of most commonly studied TiO_2 surfaces were calculated, including (001), (100), (110), (111) and (101) surfaces, as shown in Fig. S1 in the Electronic Supplementary Material (ESM). The surface with the lowest surface energy ((101), 0.2 J·m^{-2}, Fig. 1(a)) is the most stable surface and it was employed in the subsequent adsorption energy and Gibbs free energy calculations. Before calculating the adsorption energies of Li_2S_x (x = 1, 2, 4, 6, 8)/S_8 with TiO_2, the preferential adsorption sites on TiO_2 (101) plane were

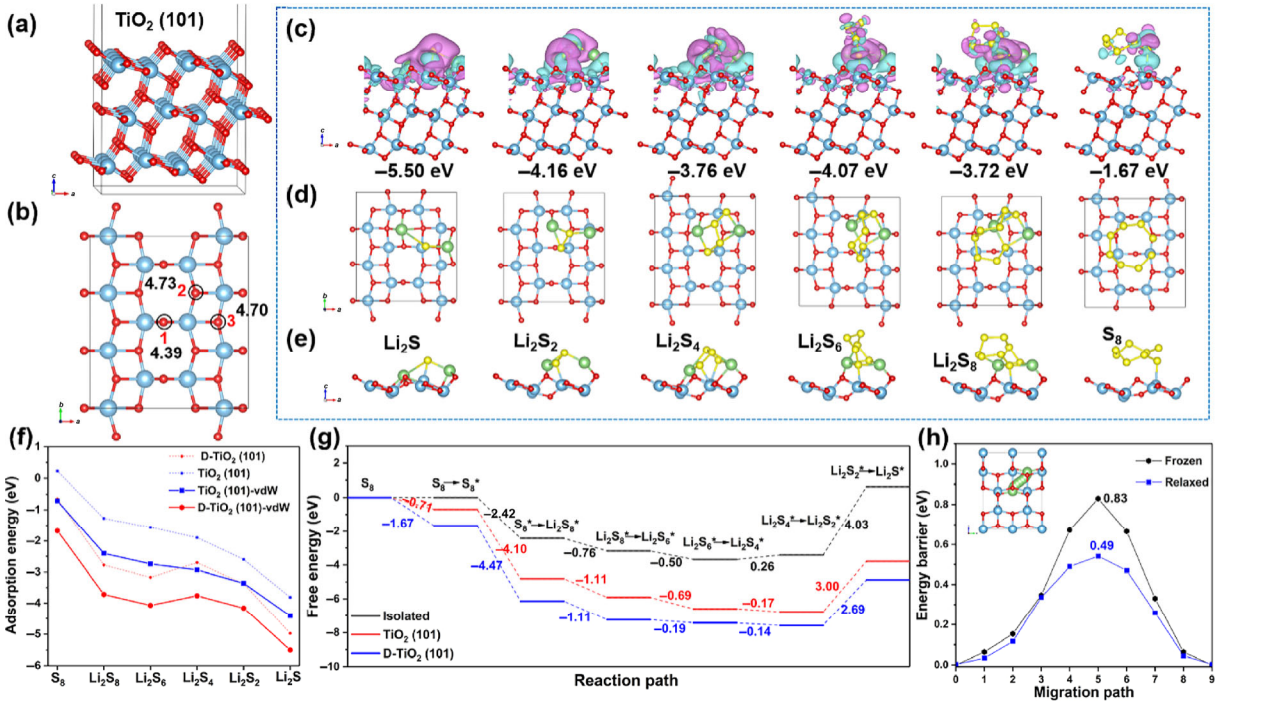

Figures 1 (a) and (b) The configuration of most stable TiO_2 (101) surface and its top layer. (The defect formation energies of oxygen at different sites are labelled aside and the unit is eV). (c) The fully optimized adsorption configurations of Li_2S_x/S_8 on D-TiO_2 (101) lattice plane with 3D differential charge contour surfaces (The iso-surface value is 0.001 e·Bohr^{-3}, and the purple surfaces refer to the electronic loss and the blue to the electronic increase; the adsorption energies are labelled below). (d) and (e) The adsorption configurations form top view and side view with partial Ti, O atoms being hided. (f) The adsorption energy plots calculated with and without vdW interaction. (g) The free energy plots of Li_2S_x/S_8 conversion reactions considered vdW interactions in isolated state, on TiO_2 (101) surface and on D-TiO_2 (101) surface, respectively. (h) The energy barrier plots of Li transport in frozen and relaxed TiO_2 bulk along the migration path shown by the insert.

tested with Li_2S. Six initial positions of Li_2S on the TiO_2 (101) plane were constructed and optimized (Fig. S2 in the ESM), among which the configuration (4) has the most negative adsorption energy. All the S-Ti bonds of different adsorption configurations are about 2.2 Å of the length, and most Li-O bonds are of ~ 1.8–2.0 Å. The topmost O atoms on TiO_2 (101) plane are the most active bonding sites to Li atoms of polysulfides. In addition, the Ti atoms have strong attractive interactions to S atoms, and sometimes the Ti atoms displaced from the equilibrium position. Based on the similar approach, the configurations for the Li_2S_x/S_8-TiO_2 (101) complexes were constructed and optimized (Fig. S3 in the ESM). The adsorption energies of Li_2S_x/S_8 on the TiO_2 (101) surface decrease with the lengthening of polysulfides chain, and it is the weakest to S_8. The DFT-D3 adsorption energies are −4.41, −3.36, −2.93, −2.74, −2.4, and −0.71 eV for Li_2S, Li_2S_2, Li_2S_4, Li_2S_6, Li_2S_8, and S_8, respectively. This is in accordance with the differential charge distribution results (Fig. S3(a) in the ESM), the more negative adsorption energy corresponds to a more massive electron change. With the strong bonding of Li to O and S to Ti, the electrons transfer from Li and Ti atoms towards O and S atoms, respectively.

Based on the above results, we have constructed several D-TiO_2 models by deleting an oxygen atom at different site on the TiO_2 (101) surface (Fig. 1(b), and Fig. S4 in the ESM), corresponding to the concentration of oxygen defects of 1.4%. The defect formation energies of oxygen at site 1, 2 and 3 are 4.39, 4.73 and 4.7 eV, respectively, indicating that the oxygen defect is most likely to be generated at site 1. The D-TiO_2 (101) defective surface with oxygen defect at site 1 also has the lowest energy compared to the other two, and we used it for the subsequent calculations. The most stable adsorption configurations of Li_2S_x/S_8 on D-TiO_2 (101) surface are shown in Figs. 1(c)–1(e) and Fig. S5 in the ESM. Although the D-TiO_2 (101) surface has one less O atom, the Li_2S_x/S_8 anchor ability has the similar trend as the defect-free TiO_2 (101) surface, and the DFT-D3 adsorption energies are −5.50, −4.16, −3.76, −4.07, −3.72, and −1.67 eV for Li_2S, Li_2S_2, Li_2S_4, Li_2S_6, Li_2S_8, and S_8, respectively (Fig. 1(f)). As we can see, the D-TiO_2 (101) surface is more active and has distinctively stronger interaction with Li_2S_x/S_8 than the defect-free TiO_2 (101) surface, showing more charge transfers and more negative adsorption energies. The O atom right below the missing O position on the D-TiO_2 surface may departure from the previous position after absorbing Li_2S_x/S_8. The percentages of vdW contributions to the adsorption energies of Li_2S_x/S_8 on D-TiO_2 and TiO_2 are shown in Fig. S6 in the ESM. It turns out that the chemical bonding effect is stronger when the polysulfides molecular is smaller. For the adsorption of S_8 on the defect-free TiO_2 (101) surface, the interaction energies almost totally come from the vdW interaction contributions (DFT-D3), otherwise it will repel S_8, whereas the D-TiO_2 (101) surface show more strong chemical interactions to S_8 but the vdW interaction contribution is still dominant. Figure 1(g) presents the free energy along the reaction path from S_8 to Li_2S. The overall free energies are 0.63, −3.78, and −4.41 eV for isolated Li_2S_x/S_8 (no TiO_2 involved), Li_2S_x/S_8 on the TiO_2 (101) surface, and Li_2S_x/S_8 on the D-TiO_2 (101) surface, respectively. These values indicate that the overall reaction on TiO_2 or D-TiO_2 surfaces is exothermic, while it is endothermic without TiO_2. In these individual steps, only the reduction of Li_2S_2 to Li_2S is apparently endothermic with a positive free energy, which means this step is the rate-limiting step. Encouragingly, D-TiO_2 can accelerate this reaction by reducing the free energy of reaction, facilitating effective transformation of S_8 to Li_2S.

To obtain a deep understanding of the effect of the oxygen vacancy and the interaction of polysulfides with D-TiO_2, the projected density of states (PDOS) of TiO_2, D-TiO_2 and their adsorption configurations with Li_2S_6 were calculated (Fig. S7 in the ESM). The top of the valence bands of TiO_2 and D-TiO_2 is dominated by the O_2p orbitals and the conduction bands are mainly contributed by Ti_3d orbitals. When an oxygen vacancy is created, the Fermi energy of TiO_2 shifts into conduction band, indicating the existance of Ti^{3+} defect states. Furthermore, the electrical conductivity of TiO_2 is increased due to the n-type semiconductor behavior [43]. D-TiO_2 also shows asymmetric distributions of spin-up electrons and spin-down ones owing to the oxygen vacancy, which demonstrate the magnetism and polarity of D-TiO_2. After absorbing Li_2S_6, the polarity of D-TiO_2 decreases, indicating the lone pair electrons of Ti participate in the bonding with Li_2S_6. The S_3p and Li_2s PDOSs of D-TiO_2_Li_2S_6 show more states on the bottom of valance band than those of TiO_2_Li_2S_6, indicating the more electrons of Li and S in D-TiO_2_Li_2S_6 transferred from anti-bonding orbitals to bonding orbitals. This result confirms the better adsorption of Li_2S_6 on D-TiO_2 than on defect-free TiO_2. Moreover, in D-TiO_2_Li_2S_6, the PDOSs of S_3p and Li_2s have better overlap with those of Ti_3d and O_2p, respectively, corresponding more feasible electron transfer and stronger interactions of S-Ti and Li-O, which is consistent with their atomic adsorption configurations and the differential charge analysis.

In addition, the transport barrier of Li inside the bulk TiO_2 has been calculated. The Li migration path displayed in Fig. S8 in the ESM has the two-dimensional "S" shape along the perspective of *a*-axis. The two ends of the pathway are spatially symmetrical sites which are the most stable sites for Li to stay. The energy barrier plots along the pathway indicate that the middle site could possibly be the most unstable site for Li, determining the overall transport energy barrier (Fig. 1(h)). The Li transport energy barrier as low as 0.49 eV in relaxed TiO_2 bulk is generally more reasonable than that of 0.83 eV in frozen TiO_2 bulk.

3.2 Experimental design and characterization of D-TiO_2@Gr

According to the above DFT calculations, D-TiO_2 is a very promising polysulfide anchoring material for LSB. Therefore, we designed D-TiO_2@Gr combining of D-TiO_2 nanosheets with 3D graphene as the sulfur host and characterized its structure and electrochemical performance. The synthesis route of D-TiO_2@Gr is illustrated in Fig. 2(a). The TiO_2@Gr aerogel was fabricated through a hydrothermal process following by freeze-drying, and the D-TiO_2@Gr aerogel was formed after the calcination of the TiO_2@Gr aerogel in a reducing atmosphere (Ar:H_2 = 95:5, v/v). In the TiO_2@Gr aerogel, the TiO_2 nanosheets are evenly and tightly attached to the Gr sheets. From the SEM measurement, the pure 3D Gr aerogel without TiO_2 possesses abundant cross-linked micro pores, while the pure TiO_2 nanosheets without the Gr severely aggregated together (Figs. S9(a) and S9(b) in the ESM). In the D-TiO_2@Gr aerogel, the porous framework of 3D Gr was well maintained while more pores were produced, and the D-TiO_2 nanosheets in rectangular shape with the edge lengths of 30–40 nm uniformly distributed on the surfaces of 3D Gr (Figs. 2(b)–2(e)). Through STEM characterizations, the high crystallinity of D-TiO_2 nanosheets is confirmed by the cloth-like imaging (Fig. 2(f)) and the ultrathin thickness of ~ 5 nm is shown by cross section imaging (Fig. 2(g)). The HRTEM image and embedded fast Fourier transform (FFT) pattern

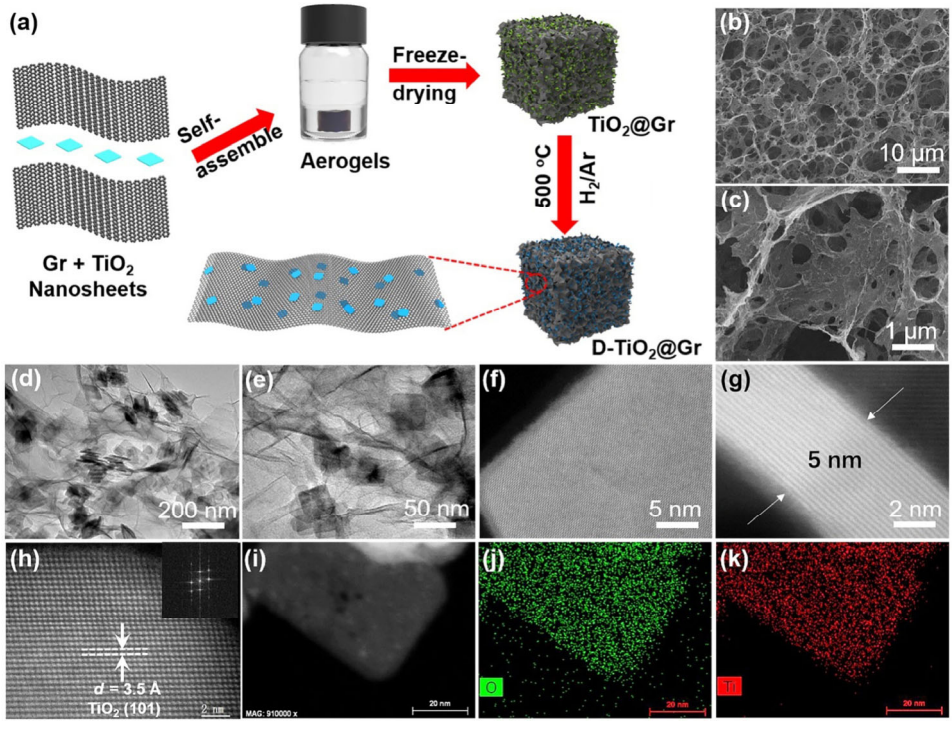

Figure 2 (a) Synthetic scheme of 3D D-TiO_2@Gr. Structural characterizations of D-TiO_2@Gr. (b) and (c) SEM images with lower resolution and higher resolution, respectively. (d) and (e) TEM images, (f) STEM images of TiO_2 sheets and (g) the magnified cross section imaging. (h) HRTEM image and the insert image is the corresponding FFT pattern. (i)–(k) STEM image with corresponding EDS mapping images.

show the highly ordered lattice fringes and the holistically well-aligned structure of the single-crystal D-TiO_2 nanosheets (Fig. 2(h)). The interplanar spacing is 3.5 Å, which is corresponding to the (101) lattice plane of anatase TiO_2. The STEM image (Fig. 2(i)) shows some black dots in the TiO_2 nanosheet surface, which indicates the presence of defects. The even elemental distribution maps of O and Ti confirm that TiO_2 is a homogeneous phase (Figs. 2(j) and 2(k))). Additionally, the EDS mapping of the D-TiO_2@Gr indicates the uniform distribution of C, Ti, and O, which further prove that the well-dispersed D-TiO_2 attached 3D graphene was obtained (Figs. S9(c)–S9(f) in the ESM).

The XRD patterns of defect-free TiO_2 and D-TiO_2@Gr are indexed to tetragonal anatase TiO_2 (PDF no. 01-071-1168). There is a weak satellite peak accompanying the diffraction peak of D-TiO_2 (101) lattice plane at ~ 25°, which is due to the slight diffraction of reduced Gr (002) lattice plane (Fig. 3(a)), and all the other diffraction peaks are at the same positions with those of TiO_2. The Raman spectrum (Fig. S10 in the ESM) of D-TiO_2 is almost overlapped with that of TiO_2, while D-TiO_2@Gr show the weak characteristic peaks of TiO_2 and the strong D, G peaks of Gr. Figure S11 in the ESM shows the TG measurement, and it turned out the mass percentage of Gr is about ~ 79.8% and the Gr pyrolyzes at temperature region of ~ 300–550 °C. The residual mass percentage of about 19.1%, which belongs to D-TiO_2. In order to confirm the existence of oxygen defects, the EPR spectra in Fig. 3(b) demonstrates that the D-TiO_2 is magnetic and the defect-free TiO_2 is nonmagnetic, which is also a proof of the existence of oxygen defects in the D-TiO_2 [19, 20, 44]. In addition, the core-level O 1s and Ti 2p XPS spectra of D-TiO_2 were also analyzed (Fig. 3(c) and Fig. S12 in the ESM), which both show an additional peak due to the oxygen defects compared with defect-free TiO_2 [37]. From the EELS comparison, we can see that oxygen defects in D-TiO_2 shift the peaks of Ti-L2,3 to the left (Fig. 3(d)).

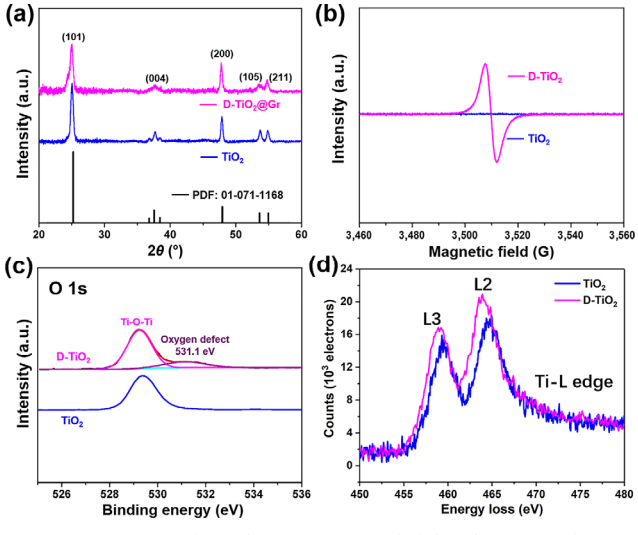

Figure 3 (a) XRD plots of D-TiO_2@Gr and defect-free TiO_2. (b) EPR spectra, (c) XPS core-level O 1s profiles, and (d) EELS Ti-L edge spectra of D-TiO_2 and defect-free TiO_2.

3.3 Electrochemical performance of D-TiO_2@Gr

We have assembled the LSB cells by using D-TiO_2@Gr as the host materials, and the active sulfur source is Li_2S_6 dissolved in electrolyte. A series of electrochemical tests of D-TiO_2@Gr were performed, with the defect-free TiO_2@Gr and Gr as control samples. The CV tests were employed to reveal the functional mechanisms of D-TiO_2@Gr during cycling (Fig. 4(a)). After the activation of the first cycle, the second and following cycles become stable. The cathodic peak located at ~ 2.29 V refers to the reduction of S_8 to long-chain Li_2S_x ($4 \le x \le 8$) and the peak located at ~ 1.97 V indicates the further reduction to short-chain Li_2S_x ($1 \le x < 4$). During the repeatable charging process, the oxidation of Li_2S to short-chain Li_2S_x appears at

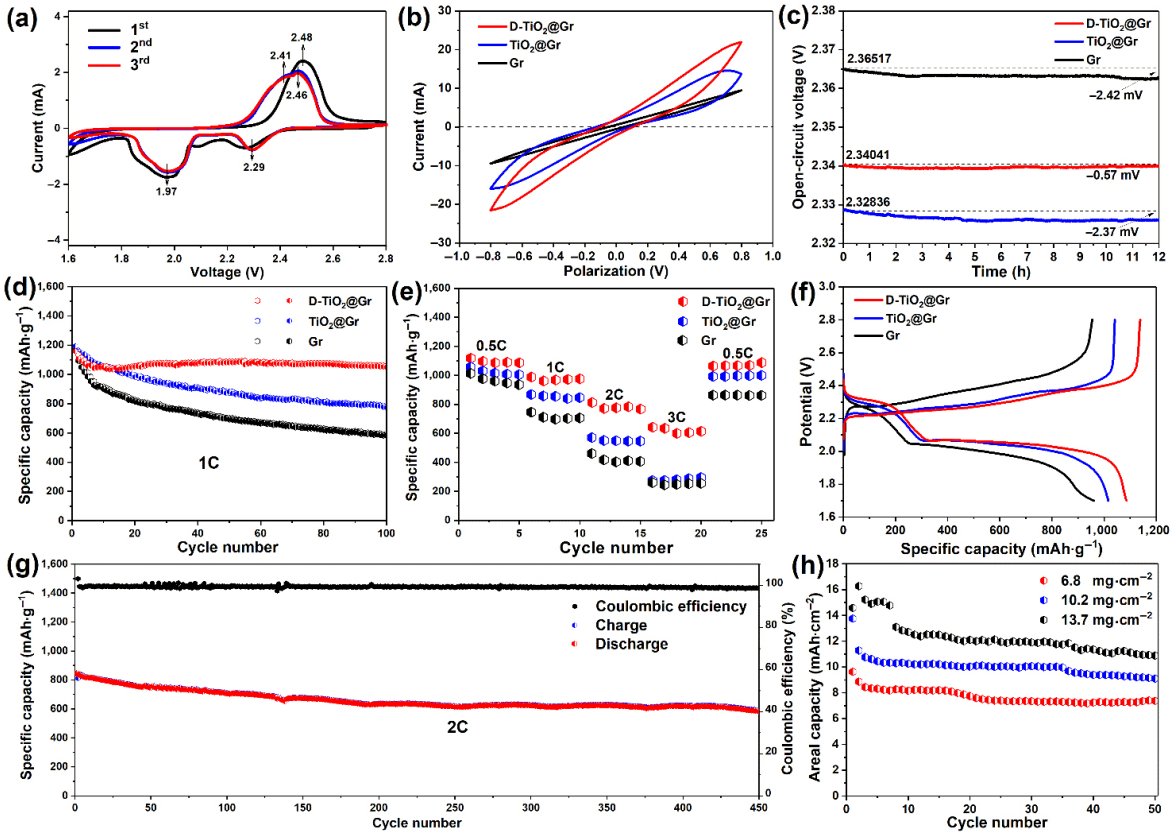

Figure 4 (a) CV curves at first 3 cycles of D-TiO_2@Gr at the scan rate of 0.1 mV·s^{-1}. (b) The CV curves of symmetric batteries with the scan rate of 80 mV·s^{-1}. (c) OCV plots, (d) cyclic curves at 1C, (e) rate curves (0.5–3C) and (f) charge-discharge curves at 0.5C of D-TiO_2@Gr, TiO_2@Gr and Gr, respectively. (g) The long-term cyclic curve of D-TiO_2@Gr at 2C. The general sulfur mass loading is 3.2 mg·cm^{-2} for different hosts. (h) Areal specific capacity changing curves at 0.2C of D-TiO_2@Gr with high mass loading of 6.8, 10.2 and 13.7 mg·cm^{-2}.

~ 2.41 V and subsequently to long-chain Li_2S_x at ~ 2.46 V. The large gap between the reduction peak and oxidation peak of short-chain Li_2S_x illustrates that the conversion of Li_2S to short-chain Li_2S_x is extremely hard. This is due in part to the intrinsic insulating property of Li_2S, and this process is even tougher for TiO_2@Gr and Gr supported cells which can be seen from the apparently larger polarization of redox peaks shown in Fig. S13(a) in the ESM. The CV curves of symmetrical cells supported by D-TiO_2@Gr, TiO_2@Gr and Gr hosts with Li_2S_6 electrolyte were tested at the voltage scan rate of 80 mV·s^{-1} within a voltage range of –0.8–0.8 V (Fig. 4(b)). D-TiO_2@Gr achieved the higher current responses than TiO_2@Gr and Gr, which means D-TiO_2 is superior to TiO_2/Gr in effectively accelerating the reaction kinetics of polysulfides [18, 45, 46]. This result is well consistent with our DFT results that the oxygen defects can promote the conversion of polysulfides. The OCVs of half-batteries with lithium foil as counter electrode were tested (Fig. 4(c)). The voltage loss of D-TiO_2@Gr after 12 h is only 0.57 mV, much lower than TiO_2@Gr and Gr (2.37 and 2.42 mV, respectively). This finding demonstrated the D-TiO_2 is of great significance to inhibit the shuttle effect inside the cell.

To measure the capacity of the D-TiO_2@Gr supported LSB, the assembled cells were charged/discharged at the current density of 1C (1,675 mA·g^{-1}). As displayed in Fig. 4(d), the initial discharge capacity is 1,158.2 mAh·g^{-1} and retained to 90.6% with a reversible capacity of 1,049.3 mAh·g^{-1} after 100 cycles, which is equivalent to the decay per cycle of only 0.094%. The TiO_2@Gr and Gr supported cells discharge the similar high initial capacities of 1,192.8 and 1,163.4 mAh·g^{-1}, but the capacity decay rates are 0.35% and 0.5%, respectively, much higher than that of D-TiO_2@Gr. Furthermore, the rate performance of a cell is also important for practical application, reflecting the electronic conductivity, ionic conductivity, and the structural stability of electrodes. The D-TiO_2@Gr electrode was successively charged/discharged at 0.5C, 1C, 2C, 3C and back to 0.5C (Fig. 4(e)). It exhibits high capacities at different current rates of 1,089.5, 971.6, 782.8, 604.7, and 1,069.0 mAh·g^{-1}, respectively. However, the TiO_2@Gr and Gr control samples released comparable capacities (1,078.6 and 1,066 mAh·g^{-1}) at 0.5C, but the capacity gap sharply increases with the increasing of current density. Notably, at the high current density of 3C, the capacity of D-TiO_2@Gr is two times greater than that of TiO_2@Gr or Gr. The charge-discharge curves at 0.5C further show that the polarization of D-TiO_2@Gr is the smallest (Fig. 4(f)). The excellent rate capacity of the D-TiO_2@Gr LSB can also be seen through the galvanostatic charge-discharge profiles at different current densities (Fig. S13(b) in the ESM), which indicate that D-TiO_2 promotes the fast reaction kinetics and good ionic/electronic conductivity. From the EIS profiles shown in Fig. S14 in the ESM, the charge transfer resistance of D-TiO_2@Gr is much lower than those of TiO_2@Gr and Gr. Furthermore, the ionic transfer resistances, in direct proportion to the slope of linear curve at lower frequency, show the same trend.

Figure 4(g) presents the longtime cycling of D-TiO_2@Gr electrode with stable cycling behavior at the current rate of 2C. The initial discharge capacity is 847.4 mAh·g^{-1} while the retention capacity is 582.4 mAh·g^{-1} after 450 cycles, leading to ultra-low fading of 0.068% per cycle. Since a high areal capacity is required to achieve for LSB to compete with commercial LIBs, it is important to test the electrochemical performance of an electrode with a high sulfur loading. As shown in Fig. 4(h)

and Fig. S15 in the ESM, when the mass loading of sulfur is 6.8 mg·cm^{-2}, the D-TiO_2@Gr electrode has an initial areal capacity of 9.6 mAh·cm^{-2} at 0.2C, and maintains at 7.4 mAh·cm^{-2} after 50 cycles. Furthermore, the high sulfur loading of 10.2 and 13.7 mg·cm^{-2} were achieved, and the cells perform with the initial capacities of 13.8 and 14.6 mAh·cm^{-2} with the retention areal capacities of 9.1 and 10.9 mAh·cm^{-2} after 50 cycles, respectively. Table S1 in the ESM summarizes the comparison of the electrochemical performances of the D-TiO_2@Gr with various titanium oxide-based sulfur host from the literature, and D-TiO_2@Gr show very competitive performance in terms of specific capacity and areal capacity.

The post processing structure and morphology characterizations of the cycled batteries are performed to prove the structural stability of D-TiO_2@Gr and its blocking capability for polysulfide. The XPS full spectra of the cycled D-TiO_2@Gr-S and the D-TiO_2@Gr before cycling show similar characteristics of the Ti, O, and C elements, while their Ti 2p core-level XPS spectra show similar chemical environment of Ti, indicating the good structural stability of D-TiO_2@Gr (Fig. S16 in the ESM). In addition, the S 2p peak in the XPS spectra of the D-TiO_2@Gr-S was deconvoluted into several peaks indexed to Li_2S_2/Li_2S, S_8 and sulfate, indicating the effective trapping of sulfur species in the D-TiO_2@Gr host and the strong chemical interaction between them [47, 48]. The SEM and TEM images of D-TiO_2@Gr-S after cycling, including all high sulfur-loading ones are shown in Fig. 5. Under the sulfur loading of 3.2 mg·cm^{-2}, the morphology of the D-TiO_2@Dr cathode shows little changes as compared to that of pre-cycling and it possesses homogeneous sulfur distributions. On the contrary, the defect-free TiO_2@Gr or Gr cathode shows obvious aggregation of micro-level sulfur particles after cycling, and the Gr cathode is almost wrapped by sulfur, which further demonstrates that D-TiO_2 plays a key role in dispersing sulfur species and catalyzing polysulfide conversion in the LSB (Fig. S17 in the ESM). In addition, with the increase of sulfur loadings to 6.8, 10.2, and 13.7 mg·cm^{-2}, the only difference noticed is the increase of the thickness of Gr sheets for the D-TiO_2@Gr cathode, and there is no accumulation of sulfur, indicating that D-TiO_2 has the ability to induce the uniform deposition of insoluble polysulfides/S_8. In summary, with the robust polysulfide immobilization and excellent catalytic capability, D-TiO_2@Gr reveals a new route for the design of the cathode host materials for LSB, especially with high sulfur loadings.

4 Conclusions

The effects of oxygen defects in TiO_2 for the enhancement of the polysulfide confining and catalytic conversion were explored by a series of DFT calculations and experiments. The first-principles calculations show that D-TiO_2 can significantly enhance the polysulfide immobilization and catalytic conversion as compared to defect-free TiO_2. The calculated adsorption energies of Li_2S_x on D-TiO_2 is much higher than those on defect-free TiO_2, especially for the most soluble Li_2S_6 and Li_2S_8. The D-TiO_2 (101) surface gives the lowest free energy of reactions for S_8 reducing to Li_2S. Based on our DFT calculations, we designed a new high-performance host material D-TiO_2@Gr for LSB by combining D-TiO_2 with the highly conductive porous 3D graphene. The D-TiO_2@Gr supported LSBs show excellent electrochemical performance. Especially with the high sulfur loading up to 13.7 mg·cm^{-2}, the D-TiO_2@Gr-S cathode shows a high areal capacity of 10.9 mAh·cm^{-2} with a good cycling stability. The oxygen defects in D-TiO_2 show significant enhancement of polysulfide immobilization and catalytic conversion, and the defect-engineering approach

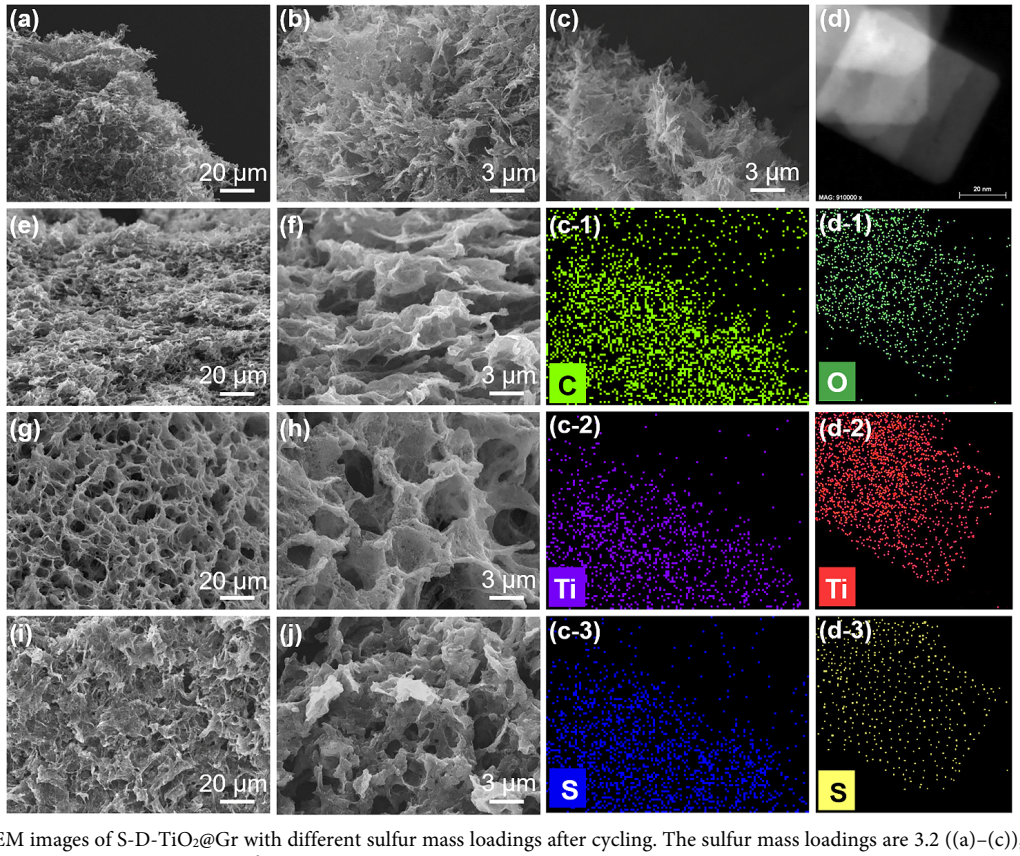

Figure 5 The SEM images of S-D-TiO_2@Gr with different sulfur mass loadings after cycling. The sulfur mass loadings are 3.2 ((a)–(c)), 6.8 ((e) and (f)), 10.2 ((g) and (h)) and 13.7 ((i) and (j)) mg·cm^{-2}, respectively. The elemental mappings of (c-1) C, (c-2) Ti, and (c-3) S are corresponds to SEM image (c). (d) The SEM image of D-TiO_2 nanosheets separated from D-TiO_2@Gr after cycling with sulfur mass loading of 3.2 mg·cm^{-2} and the elemental mappings of (d-1) O, (d-2) Ti, and (d-3) S.

provides an alternative strategy for developing new functional materials for the high-performance LSB system.

Acknowledgements

This work was supported by the Excellent Dissertation Cultivation Funds of Wuhan University of Technology (No. 2018-YS-013).

Electronic Supplementary Material: Supplementary material (further details of the DFT calculations, the SEM measurements, Raman spectra, electrochemistry measurements and performance comparison table) is available in the online version of this article at https://doi.org/10.1007/s12274-020-2850-5.

References

[1] Kim, H.; Lee, J.; Ahn, H.; Kim, O.; Park, M. J. Synthesis of three-dimensionally interconnected sulfur-rich polymers for cathode materials of high-rate lithium-sulfur batteries. *Nat. Commun.* **2015**, *6*, 7278.

[2] Manthiram, A.; Chung, S. H.; Zu, C. X. Lithium-sulfur batteries: Progress and prospects. *Adv. Mater.* **2015**, *27*, 1980–2006.

[3] Son, Y.; Lee, J. S.; Son, Y.; Jang, J. H.; Cho, J. Recent advances in lithium sulfide cathode materials and their use in lithium sulfur batteries. *Adv. Energy Mater.* **2015**, *5*, 1500110.

[4] Yang, Y.; Zheng, G. Y.; Cui, Y. Nanostructured sulfur cathodes. *Chem. Soc. Rev.* **2013**, *42*, 3018–3032.

[5] Guo, W.; Fu, Y. Z. A perspective on energy densities of rechargeable Li-S batteries and alternative sulfur-based cathode materials. *Energy Environ. Mater.* **2018**, *1*, 20–27.

[6] Yu, T.; Li, F.; Liu, C. Y.; Zhang, S. T.; Xu, H. Y.; Yang, G. C. Understanding the role of lithium sulfide clusters in lithium–sulfur batteries. *J. Mater. Chem. A* **2017**, *5*, 9293–9298.

[7] Xu, R.; Lu, J.; Amine, K. Progress in mechanistic understanding and characterization techniques of Li-S batteries. *Adv. Energy Mater.* **2015**, *5*, 1500408.

[8] He, Y. B.; Chang, Z.; Wu, S. C.; Zhou, H. S. Effective strategies for long-cycle life lithium-sulfur batteries. *J. Mater. Chem. A* **2018**, *6*, 6155–6182.

[9] Fu, A.; Wang, C. Z.; Pei, F.; Cui, J. Q.; Fang, X. L.; Zheng, N. F. Recent advances in hollow porous carbon materials for lithium-sulfur batteries. *Small* **2019**, *15*, 1804786.

[10] Ogoke, O.; Wu, G.; Wang, X. L.; Casimir, A.; Ma, L.; Wu, T. P.; Lu, J. Effective strategies for stabilizing sulfur for advanced lithium-sulfur batteries. *J. Mater. Chem. A* **2017**, *5*, 448–469.

[11] Pang, Q.; Liang, X.; Kwok, C. Y.; Nazar, L. F. Advances in lithium-sulfur batteries based on multifunctional cathodes and electrolytes. *Nat. Energy* **2016**, *1*, 16132.

[12] Wu, Y. L.; Zhu, X. R.; Li, P. R.; Zhang, T.; Li, M.; Deng, J.; Huang, Y.; Ding, P.; Wang, S. X.; Zhang, R. et al. Ultradispersed W_xC nanoparticles enable fast polysulfide interconversion for high-performance Li-S batteries. *Nano Energy* **2019**, *59*, 636–643.

[13] Yu, M. L.; Zhou, S.; Wang, Z. Y.; Wang, Y. W.; Zhang, N.; Wang, S.; Zhao, J. J.; Qiu, J. S. Accelerating polysulfide redox conversion on bifunctional electrocatalytic electrode for stable Li-S batteries. *Energy Storage Mater.* **2018**, *20*, 98–107.

[14] Du, L. Y.; Wu, Q.; Yang, L. J.; Wang, X.; Che, R. C.; Lyu, Z.; Chen, W.; Wang, X. Z.; Hu, Z. Efficient synergism of electrocatalysis and physical confinement leading to durable high-power lithium-sulfur batteries. *Nano Energy* **2019**, *57*, 34–40.

[15] Xu, L. L.; Zhao, H. Y.; Sun, M. Z.; Huang, B. L.; Wang, J. W.; Xia, J. L.; Li, N.; Yin, D. D.; Luo, M.; Luo, F. et al. Oxygen vacancies on layered niobic acid that weaken the catalytic conversion of polysulfides in lithium-sulfur batteries. *Angew Chem., Int. Ed.* **2019**, *58*, 11491–11496.

[16] Yu, M. L.; Wang, Z. Y.; Wang, Y. W.; Dong, Y. F.; Qiu, J. S. Freestanding flexible Li_2S paper electrode with high mass and capacity loading for high-energy Li-S batteries. *Adv. Energy Mater.* **2017**, *7*, 1700018.

[17] Peng, H. J.; Huang, J. Q.; Cheng, X. B.; Zhang, Q. Review on high-loading and high-energy lithium-sulfur batteries. *Adv. Energy Mater.* **2017**, *7*, 1700260.

[18] Yang, W.; Yang, W.; Dong, L. B.; Gao, X. C.; Wang, G. X.; Shao, G. J. Enabling immobilization and conversion of polysulfides through a nitrogen-doped carbon nanotubes/ultrathin MoS_2 nanosheet core-shell architecture for lithium-sulfur batteries. *J. Mater. Chem. A* **2019**, *7*, 13103–13112.

[19] Salhabi, E. H. M.; Zhao, J. L.; Wang, J. Y.; Yang, M.; Wang, B.; Wang, D. Hollow multi-shelled structural TiO_{2-x} with multiple spatial confinement for long-life lithium-sulfur batteries. *Angew. Chem., Int. Ed.* **2019**, *58*, 9078–9082.

[20] Wang, H. E.; Yin, K. L.; Qin, N.; Zhao, X.; Xia, F. J.; Hu, Z. Y.; Guo, G. L.; Cao, G. Z.; Zhang, W. J. Oxygen-deficient titanium dioxide as a functional host for lithium-sulfur batteries. *J. Mater. Chem. A* **2019**, *7*, 10346–10353.

[21] Cai, W. L.; Li, G. R.; Zhang, K. L.; Xiao, G. N.; Wang, C.; Ye, K. F.; Chen, Z. W.; Zhu, Y. C.; Qian, Y. T. Conductive nanocrystalline niobium carbide as high-efficiency polysulfides tamer for lithium-sulfur batteries. *Adv. Funct. Mater.* **2018**, *28*, 1704865.

[22] Hao, B. Y.; Li, H.; Lv, W.; Zhang, Y. B.; Niu, S. Z.; Qi, Q.; Xiao, S. J.; Li, J.; Kang, F. Y.; Yang, Q. H. Reviving catalytic activity of nitrides by the doping of the inert surface layer to promote polysulfide conversion in lithium-sulfur batteries. *Nano Energy* **2019**, *60*, 305–311.

[23] Li, C. C.; Liu, X. B.; Zhu, L.; Huang, R. Z.; Zhao, M. W.; Xu, L. Q.; Qian, Y. T. Conductive and polar titanium boride as a sulfur host for advanced lithium-sulfur batteries. *Chem. Mater.* **2018**, *30*, 6969–6977.

[24] Guan, B.; Fan, L. S.; Wu, X.; Wang, P. X.; Qiu, Y.; Wang, M. X.; Guo, Z. K.; Zhang, N. Q.; Sun, K. N. The facile synthesis and enhanced lithium-sulfur battery performance of an amorphous cobalt boride (Co_2B)@graphene composite cathode. *J. Mater. Chem. A* **2018**, *6*, 24045–24049.

[25] Chen, Y.; Zhang, W. X.; Zhou, D.; Tian, H. J.; Su, D. W.; Wang, C. Y.; Stockdale, D.; Kang, F. Y.; Li, B. H.; Wang, G. X. Co-Fe mixed metal phosphide nanocubes with highly interconnected-pore architecture as an efficient polysulfide mediator for lithium-sulfur batteries. *ACS Nano* **2019**, *13*, 4731–4741.

[26] Razaq, R.; Sun, D.; Xin, Y.; Li, Q.; Huang, T. Z.; Zheng, L.; Zhang, Z. L.; Huang, Y. H. Enhanced kinetics of polysulfide redox reactions on Mo_2C/CNT in lithium-sulfur batteries. *Nanotechnology* **2018**, *29*, 295401.

[27] Wang, J. W.; Zhou, B.; Zhao, H. Y.; Wu, M. M.; Yang, Y. D.; Sun, X. L.; Wang, D. H.; Du, Y. P. A sandwich-type sulfur cathode based on multifunctional ceria hollow spheres for high-performance lithium–sulfur batteries. *Mater. Chem. Front.* **2019**, *3*, 1317–1322.

[28] Zhou, T. H.; Lv, W.; Li, J.; Zhou, G. M.; Zhao, Y.; Fan, S. X.; Liu, B. L.; Li, B. H.; Kang, F. Y.; Yang, Q. H. Twinborn TiO_2-TiN heterostructures enabling smooth trapping-diffusion-conversion of polysulfides towards ultralong life lithium-sulfur batteries. *Energy Environ. Sci.* **2017**, *10*, 1694–1703.

[29] Song, Y. Z.; Zhao, W.; Kong, L.; Zhang, L.; Zhu, X. Y.; Shao, Y. L.; Ding, F.; Zhang, Q.; Sun, J. Y.; Liu, Z. F. Synchronous immobilization and conversion of polysulfides on a VO_2-VN binary host targeting high sulfur load Li-S batteries. *Energy Environ. Sci.* **2018**, *11*, 2620–2630.

[30] Choudhury, B.; Bayan, S.; Choudhury, A.; Chakraborty, P. Narrowing of band gap and effective charge carrier separation in oxygen deficient TiO_2 nanotubes with improved visible light photocatalytic activity. *J. Colloid Interf. Sci* **2016**, *465*, 1–10.

[31] Liu, M. M; Zhang, C. C.; Su, J. M.; Chen, X.; Ma, T. Y.; Huang, T.; Yu, A. S. Propelling polysulfide conversion by defect-rich MoS_2 nanosheets for high-performance lithium-sulfur batteries. *ACS Appl. Mater. Interfaces* **2019**, *11*, 20788–20795.

[32] Tian, Y.; Zhao, Y.; Zhang, Y. G.; Ricardez-Sandoval, L. A.; Wang, X.; Li, J. D. Construction of oxygen-deficient $La(OH)_3$ nanorods wrapped by reduced graphene oxide for polysulfide trapping toward high-performance lithium/sulfur batteries. *ACS Appl. Mater. Interfaces* **2019**, *11*, 23271–23279.

[33] Wang, Y. K.; Zhang, R. F.; Chen, J.; Wu, H.; Lu, S. Y.; Wang, K.; Li, H. L.; Harris, C. J.; Xi, K.; Kumar, R. V. et al. Enhancing catalytic

activity of titanium oxide in lithium-sulfur batteries by band engineering. *Adv. Energy Mater.* **2019**, *9*, 1900953.

[34] Chen, X.; Hou, T. Z.; Persson, K. A.; Zhang, Q. Combining theory and experiment in lithium–sulfur batteries: Current progress and future perspectives. *Mater. Today* **2019**, *22*, 142–158.

[35] Rana, M.; Li, M.; Huang, X.; Luo, B.; Gentle, I.; Knibbe, R. Recent advances in separators to mitigate technical challenges associated with re-chargeable lithium sulfur batteries. *J. Mater. Chem. A* **2019**, *7*, 6596–6615.

[36] Hummers, W. S. Jr., Offeman, R. E. Preparation of graphitic oxide. *J. Am. Chem. Soc.* **1958**, *80*, 1339.

[37] Wan, J. W.; Chen, W. X.; Jia, C. Y.; Zheng, L. R.; Dong, J. C.; Zheng, X. S.; Wang, Y.; Yan, W. S.; Chen, C.; Peng, Q. et al. Defect effects on TiO_2 nanosheets: Stabilizing single atomic site Au and promoting catalytic properties. *Adv. Mater.* **2018**, *30*, 1705369.

[38] Kresse, G.; Furthmüller, J. Efficient iterative schemes for *ab initio* total-energy calculations using a plane-wave basis set. *Phys. Rev. B* **1996**, *54*, 11169–11186.

[39] Perdew, J. P.; Burke, K.; Ernzerhof, M. Generalized gradient approximation made simple. *Phys. Rev. Lett.* **1996**, *77*, 3865–3868.

[40] Kresse, G.; Joubert, D. From ultrasoft pseudopotentials to the projector augmented-wave method. *Phys. Rev. B* **1999**, *59*, 1758–1775.

[41] Grimme, S.; Antony, J.; Ehrlich, S.; Krieg, H. A consistent and accurate *ab initio* parametrization of density functional dispersion correction (DFT-D) for the 94 elements H-Pu. *J. Chem. Phys.* **2010**, *132*, 154104.

[42] Henkelman, G.; Uberuaga, B. P.; Jónsson, H. A climbing image nudged elastic band method for finding saddle points and minimum energy paths. *J. Chem. Phys.* **2000**, *113*, 9901–9904.

[43] Savva, A. I.; Smith, K. A.; Lawson, M.; Croft, S. R.; Weltner, A. E.; Jones, C. D.; Bull, H.; Simmonds, P. J.; Li, L.; Xiong, H. Defect generation in TiO_2 nanotube anodes via heat treatment in various atmospheres for lithium-ion batteries. *Phys. Chem. Chem. Phys.* **2018**, *20*, 22537–22546.

[44] Sarkar, A.; Khan, G. G. The formation and detection techniques of oxygen vacancies in titanium oxide-based nanostructures. *Nanoscale* **2019**, *11*, 3414–3444.

[45] Li, B. Q.; Peng, H. J.; Chen, X.; Zhang, S. Y.; Xie, J.; Zhao, C. X.; Zhang, Q. Polysulfide electrocatalysis on framework porphyrin in high-capacity and high-stable lithium-sulfur batteries. *CCS Chem.* **2019**, *1*, 128–137.

[46] Gao, X. J.; Yang, X. F.; Li, M. S.; Sun, Q.; Liang, J. N.; Luo, J.; Wang, J. W.; Li, W. H.; Liang, J. W.; Liu, Y. L. et al. Cobalt-doped SnS_2 with dual active centers of synergistic absorption-catalysis effect for high-S loading Li-S batteries. *Adv. Funct. Mater.* **2019**, *29*, 1806724.

[47] Cai, D.; Lu, M. J.; Li, L.; Cao, J. M.; Chen, D.; Tu, H. R.; Li, J. Z.; Han, W. A highly conductive MOF of graphene analogue $Ni_3(HITP)_2$ as a sulfur host for high-performance lithium–sulfur batteries. *Small* **2019**, *15*, 1902605.

[48] Liu, S. F.; Ji, X.; Yue, J.; Hou, S.; Wang, P. F.; Cui, C. Y.; Chen, J.; Shao, B. W.; Li, J. R.; Han, F. D. et al. High interfacial-energy interphase promoting safe lithium metal batteries. *J. Am. Chem. Soc.* **2020**, *142*, 2438–2447.